Influence of Slip on the Rayleigh-Plateau Rim Instability in Dewetting Viscous Films

Oliver Bäumchen,[1,†] Ludovic Marquant,[1] Ralf Blossey,[2] Andreas Münch,[3] Barbara Wagner,[4] and Karin Jacobs[1,*]
[1]Saarland University, Department of Experimental Physics, Campus, D-66123 Saarbrücken, Germany
[2]Interdisciplinary Research Institute (IRI), CNRS USR 3078, 59658 Villeneuve d'Ascq, France
[3]Mathematical Institute, University of Oxford, Oxford OX2 6GG, United Kingdom
[4]Technical University of Berlin, Institute for Mathematics, D-10623 Berlin, Germany
(Received 11 October 2013; published 2 July 2014)

A dewetting viscous film develops a characteristic fluid rim at its receding edge due to mass conservation. In the course of the dewetting process, the rim becomes unstable via an instability of Rayleigh-Plateau type. An important difference exists between this classic instability of a liquid column and the rim instability in a thin film as the growth of the rim is continuously fueled by the receding film. We explain how the development and macroscopic morphology of the rim instability are controlled by the slip of the film on the substrate. A single thin-film model captures quantitatively the characteristics of the complete evolution of the rim observed in the experiments.

DOI: 10.1103/PhysRevLett.113.014501 PACS numbers: 47.15.gm, 47.20.-k, 83.50.Lh, 83.80.Sg

One of the best-studied liquid instabilities is the Rayleigh-Plateau instability of a liquid column which, e.g., underlies the breakup of water flowing out of a faucet [1–4]. Dewetting thin viscous (e.g., polymeric) films display variations of this classic instability and have received ample attention in recent years from both experiment [5–11] and theory [12–14]. In thin film flows [15,16], significant additional physical processes are involved as compared to classical liquid setups: (i) in addition to intermolecular forces driving dewetting [17], slip on the substrate [18–20], viscous and even viscoelastic effects [21] may matter; (ii) the retraction of the dewetting front leads to a continuous growth of the rim due to mass conservation while the rim as a whole is pulled across the substrate. The interaction between the liquid in the rim and the substrate is thus of particular importance in these systems. The quantification and the nature of slip is intensively discussed in the literature [22,23]. Its presence strongly impacts lab-on-a-chip technologies [24], e.g., via the reduction of dispersion and the enhancement of throughput in microfluidic channels [25]. Here we demonstrate the decisive role interfacial slip has for the rim instability in viscous films and link characteristic, optically visible features to microscopic slip at the solid-liquid interface. We present a single thin-film model that quantitatively captures the complete evolution of the rim, from the initial perturbations to the formation of fingers.

Figure 1 shows an experimental observation of the rim instability as it arises in a dewetting thin film on two types of substrates (upper and lower row). The edge of the receding thin film moves from the left to the right. Its position is given by the dewetted distance $D(t)$. Comparing different films of equal film thickness at identical D ensures identical volume in the rims. A linear geometry has been chosen which bears the advantage that no geometrical restriction on the wavelength of the instability along the rim is imposed, in contrast to equivalent processes at the circumference of holes [10,11] or rings [26,27]. Upon advancing, the rim accumulates the dewetted material and in the course of this process passes continuously through three regimes: (I) undulations develop along the rim; (II) the undulations grow into bulges; (III) bulges emerge into fingers ("fingering") whose necks can develop an own Rayleigh-Plateau—type instability. In the upper row of Fig. 1, the film passes all three regimes (a) and bulges exhibit an asymmetric shape (c), whereby, for the same range of dewetted distance, the film in the bottom row does not reach the fingering regime (b) and bulges are symmetric (d).

Both dewetting processes in Fig. 1 feature viscous films of thickness $H \sim 100$ nm, but they evolve on two surfaces with different slip properties, as characterized by a slip length b [28]. The slip length represents the length below the solid-liquid interface where the flow velocity profile extrapolates to zero. The substrates are Si wafers (Siltronic) that were hydrophobized either by the preparation of a dodecyl-trichlorosilane (DTS) self-assembled monolayer [29] or by spin- or dip-coating an amorphous fluoropolymer layer (AF1600, Aldrich). On AF1600 (bottom row of Fig 1), the liquid films in this study reveal small slip lengths in the range of $b \approx 0.04$ μm, whereas on DTS (upper row in Fig. 1) the exact same films exhibit slip lengths in the range of 1 μm, i.e., $b \gg H$. The slip lengths have been determined using the rim profile analysis method [30–33] and rationalized by a combined x-ray and neutron reflectivity study [34]. Structural details, surface roughness values, and wetting properties of the coatings are given in Ref. [35].

The viscous liquid in this study is unentangled atactic polystyrene (PS, purchased from PSS). The molecular

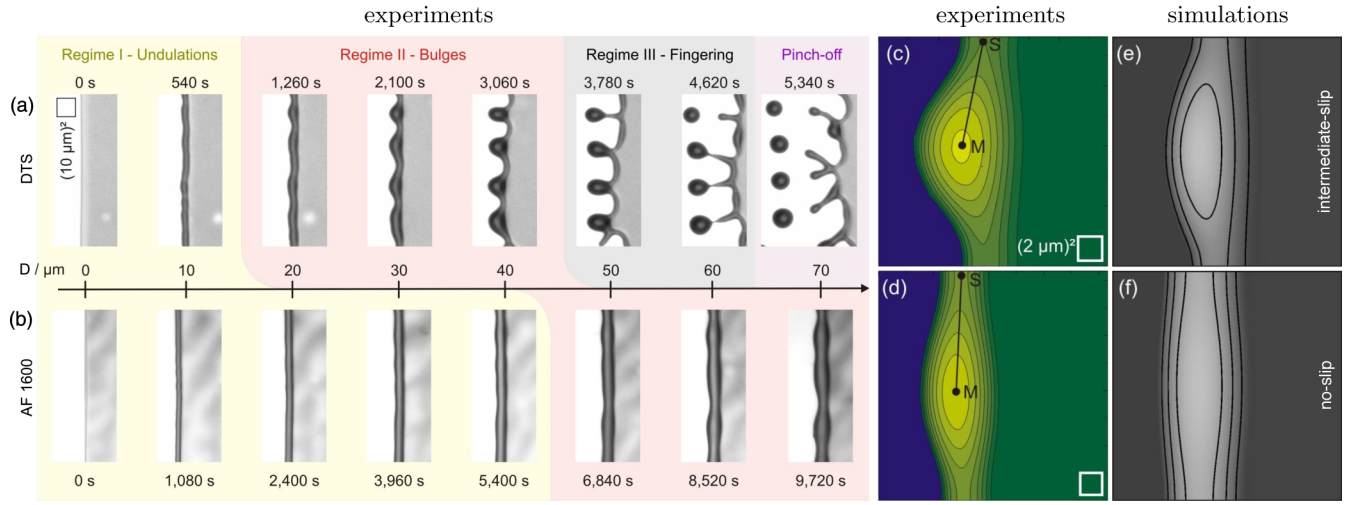

FIG. 1 (color online). (a),(b) Dewetting of a thin viscous film of PS on DTS (top) and on AF1600 (bottom), at 120 °C, by retraction of an initially straight front (13.7 kg/mol, $H = 125(5)$ nm) as seen by optical microscopy. A semicylindrical liquid rim is formed by the accumulation of liquid material (dark grey). The advance of the front is characterized by the dewetted distance $D(t)$. (c),(d) AFM top-view images of a typical bulge on DTS (c) at $D(t) = 39(2)$ μm and AF1600 (d) at $D(t) = 45(3)$ μm. (e),(f) Top-view 3D numerical simulations for intermediate-slip (e) and no-slip (f) boundary conditions [13], which match the respective experimental bulge morphology. M is the position of the highest point in the contour line plots, S the saddle point. Isoheight lines are set to each 200 nm. In the numerical results, the bulge width has been scaled to one.

weights M_w of all experiments are 10.3 or 13.7 kg/mol (polydispersity index $M_w/M_n = 1.03$) and, thus, well below the critical value for chain entanglements. Films were prepared by spin-casting a toluene (Selectipur or LiChrosolv, Merck) solution of PS on freshly cleaved mica sheets. Subsequently, the films were floated onto an ultrapure water (Milli-Q synthesis system, Millipore, organic impurities < 6 ppb, resistance at 25 °C: 18.2 MΩ cm) surface and picked up with (freshly cleaned) hydrophobized Si wafers exhibiting a native oxide layer. Dewetting of retracting straight fronts was monitored *in situ* by optical microscopy on a heating plate (Linkam) as well as *ex situ* by atomic force microscopy (AFM, ICON and Dimension 3100, Bruker), respectively. The dewetted distance was typically obtained from optical microscopy images; in AFM experiments the dewetted distance can also be calculated from three-dimensional scans of the rim based on volume conservation. Values resulting from both approaches have been checked to be in excellent agreement.

The experimental results can be described by thin-film models that are derived consistently from the Navier-Stokes equations for an incompressible liquid [13,41]: If the slip length $b = 0$ (or $b \ll H$), the film flow profile is semi-parabolic, and the dynamics corresponds to a weak-slip regime. If $b \gg H$, the dynamics corresponds to plug flow, which arises in two subregimes, depending on whether extensional stresses in the film become as important as shear stresses. If only shear stresses matter, the flow regime is called the intermediate-slip regime and otherwise the strong-slip regime. These different regimes can be represented by a single thin-film model for the height profile h, covering the respective limits. For simplicity, we give the model here in 2D, i.e., the cross section of the height profile $h(x,t)$ over substrate coordinate x and in time t:

$$\partial_t h = -\partial_x(hu),$$
$$\frac{u}{bh} = \frac{4\epsilon^2}{h}\left(1+\frac{h}{2b}\right)\partial_x(h\partial_x u) + \left(1+\frac{h}{3b}\right)\partial_x(\partial_{xx}h - \phi'(h)). \quad (1)$$

The weak-slip regime is recovered as the small lubrication parameter $\epsilon \to 0$ in Eq. (1). The strong-slip regime is obtained for the slip length parameter of order of magnitude $b = O(\beta/\epsilon^2)$, the rescaled lateral velocity $u = u^*/\epsilon^2$, and the rescaled time scale $t = \epsilon^2 t^*$ in the asymptotic limit as $\epsilon \to 0$. We also note that the well-known no-slip regime is obtained as a special case of the weak-slip regime as $b = 0$ and the intermediate-slip regime represents the asymptotic limit of the weak- and the strong-slip regime for $1 \ll O(b) \ll O(\epsilon^{-2})$. The simulations of these equations were adapted to the experimental system via the reconstructed effective interface potential $\phi(h)$, given in Ref. [17], as detailed in Ref. [35].

For the numerical calculations we use an (unperturbed) approach with the thin-film models in 2D, and, to capture the morphological details of the bulges as they emerge from small initial perturbations, we also carried out numerical computations with the full nonlinear 3D versions of the no-slip and intermediate-slip thin-film models (given for example in Ref. [13]). In Figs. 1(c)—1(f), we present the comparison of our experimental AFM data of the bulge

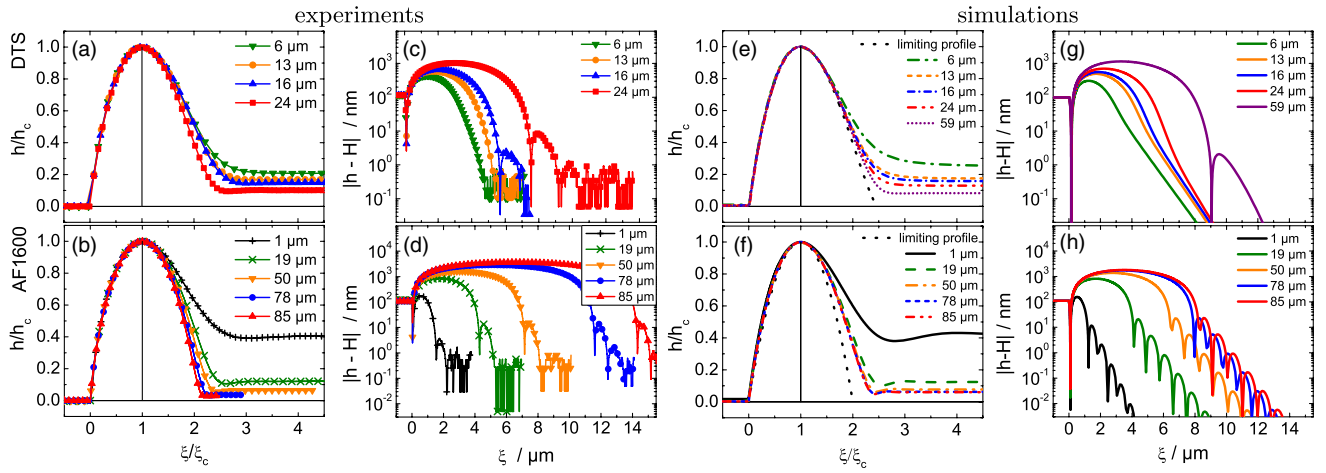

FIG. 2 (color online). (a)—(d) AFM scans of rim profiles of straight fronts of a thin film (PS(10.3 kg/mol), $H = 115(5)$ nm) on DTS [(a),(c)] at 110 °C and AF1600 [(b),(d)] at 120 °C, recorded at various travelled distances D as noted in the legend. (e)—(h) Snapshots of the unperturbed numerical simulations taken at the travelled distance D given by the experiments in (a)–(d). Normalized h, ξ with the coordinates at maximum h_c, ξ_c illustrate the approach to an asymptotic profile. The vertical straight line helps to visualize the asymmetry between the front and rear of the ridge. On DTS, the semilogarithmic representation of $|h - H|$ indicates the transition from a monotonically decaying tail to an oscillatory decay. In the presence of slip, both experiments on DTS and numerical calculations of the strong-slip model show a morphological transition of the rim profile [45]. On AF1600, oscillatory profiles are present right from the early stage ($D = 1$ μm) of the dewetting process [46].

evolution with 3D numerical calculations (using the full equations for wave numbers that are unstable according to the linear stability theory) based on the corresponding thin-film equations for both substrates, DTS and AF1600. An asymptotic analysis of the thin-film model shows that the no-slip regime leads to symmetric [Fig. 1(f)] and the intermediate-slip regime to asymmetric bulges [Fig. 1(e)] [13]. The latter is a consequence of the dependence of the dewetting velocity on the rim width in case of slip: wider sections of the rim retract more slowly than narrower sections [6]. This can easily be observed in Fig. 1(a), where the rim instability along with the velocity differences lead to fingering on the slip substrate.

Comparing the time scales in Figs. 1(a) and 1(b) at identical dewetted distance, the dewetting velocity is clearly larger in the slip case (DTS) [35]. Even if we increase the temperature (i.e., decrease the viscosity) in the no-slip case to provoke much higher dewetting velocities than on DTS in Fig. 1(a), the morphological features persist [35] and are clearly determined by slippage. The results and the scaling behavior corroborate those previously found for the growth of holes in thin films [33,42].

Aside from the morphology of the instability and the dewetting dynamics, a third fingerprint is the evolution of the rim shape, in particular how the rim merges into the flat film ahead of its motion. For the DTS substrate, the rim changes from a monotonic decay towards the flat film into an oscillatory profile during its evolution at long times [Figs. 2(a) and 2(c)]. By contrast, for AF1600 the rim profile is oscillatory right from the beginning [Figs. 2(b) and 2(d)], as expected for no-slip and also for weak-slip substrates [30]. Such a transition from a monotonic to an oscillatory rim decay exists only for the strong-slip model and is shown in Figs. 2(e) and 2(g): The approach to the asymptotic regime depends strongly on the magnitude of b. The asymptotic dynamics of the dewetting rim is generally governed by the intermediate-slip case. In this limit, the rim acquires a limiting profile of asymmetric shape [dotted black line in Fig. 2(e)] which asymptotically touches down to 0 at $\xi_e \approx 2.5\xi_c$, where ξ is the substrate coordinate in the comoving frame and ξ_c is the position of the maximum of the rim. The distance ξ_e–ξ_c, therefore, is a measure of the asymptotic (a)symmetry of the dewetting rim. For the rim profiles on AF1600, the oscillatory behavior is clearly observed in both experiment [Figs. 2(b) and 2(d)] and theory [Figs. 2(f) and 2(h)] and the rim profile in this case converges to a symmetric profile, $\xi_e \approx 2\xi_c$ [Fig. 2(f)], as expected for no-slip substrates [43]. The limiting profiles are the long time limits of the rim in the 2D intermediate and no-slip models, as determined in Refs. [13,44].

We now turn from the rim shape in 2D to its undulation along the rim in 3D, characterized by its wavelength λ, cf. Fig. 3(a). As shown in Fig. 3(c), the observed wavelength λ first grows in time as a function of dewetted distance $D(t)$ until the film enters the fingering regime (III) for which the wavelength is fixed. The undulatory instability displays a universal characteristics which is demonstrated by plotting the Rayleigh ratio, $C = \lambda/W$ where W is rim width. C is constant, see Fig. 3(d). The reference line is the theoretical result for C obtained from the intermediate-slip model and is given by $C \approx 2.4$ for the dominant wavelength [13].

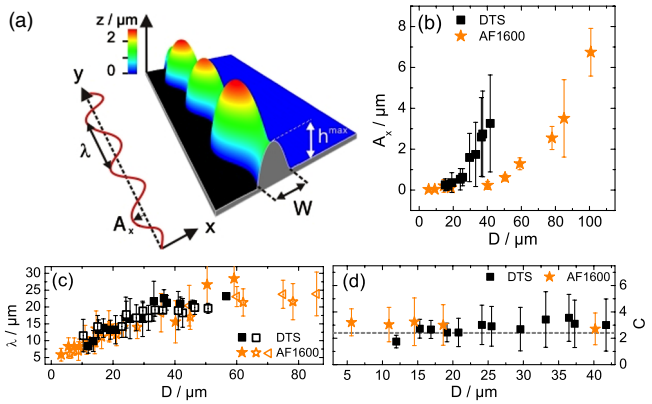

FIG. 3 (color online). (a) AFM image of an undulated rim (10.3 kg/mol at 125 °C on AF1600, $D = 97$ μm, $t = 6360$ s, scan size: 15 μm × 90 μm) with parameters characterizing the undulation: rim width W, rim height $h^{\max}$, wavelength λ, and lateral amplitude A_x. (b) Lateral amplitude A_x of the rim instability in regime I and II determined from AFM images of a PS film (10.3 kg/mol, $H = 115(5)$ nm, 120 °C) show distinct differences on DTS and AF1600. (c) For the studied film thicknesses $H = 110$–130 nm and molecular weights (10.3 and 13.7 kg/mol), represented by different symbols, the wavelength λ of the instability grows continuously with dewetted distance D and does not depend on the substrate. (d) The Rayleigh ratio $C = \lambda/W$ (where W was precisely determined from AFM images, filled symbols) as a function of D for, both, DTS and AF1600 shows a good agreement between experiments and theory (dashed line) [13].

The difference between retracting liquid fronts on DTS and AF1600 lies in the rise time of bulge growth, which is controlled by the interfacial slip. This effect can be estimated by a simple extension [35] of a model for liquid rim undulations put forward previously by Brochard-Wyart and Redon (BWR) [12]: A larger slip length imposes a shorter rise time τ_q, including a shorter rise time of the dominant mode. In order to compare this theoretical prediction to our experiments, we recorded the lateral amplitude A_x of the instability on both substrates, cf. Fig. 3(b). At identical dewetted distance, the growth of A_x is significantly faster on DTS compared to the same viscous film on AF1600. However, the fastest growing wavelength λ for the dominant mode remains unaffected by slip, as validated by the experimental results shown in Fig. 3(c).

As mentioned at the beginning, polymer films under shear may also exhibit viscoelastic properties. In the cases we studied, viscoelastic effects in the film are entirely absent as the shear rates $\dot{\gamma}$ are low and the molecular weights are chosen well below the entanglement length. Thus, the longest relaxation times τ_{rel} of the polymers are orders of magnitude shorter than the time frame of the experiments [33]. Therefore, we would like to stress the difference of our results to those obtained earlier by Gabriele *et al.* [21]: In the terminology of Gabriele *et al.*, the films are always in a relaxed (or "mature") regime and do not have to pass through an elastic regime before the undulation instability appears. Finally, we also note that the surface tension of the liquid is uniform and, thus, Marangoni effects are not present. The undulation instability is a purely hydrodynamic effect, whose appearance (but not whose presence) is controlled by the slip length b. The experimental and numerical results presented here are thus valid for all Newtonian liquids, i.e., for Weissenberg numbers $\mathrm{Wi} = \tau_{\mathrm{rel}}\dot{\gamma} \ll 1$.

In conclusion, we have shown that the appearance of the Rayleigh-Plateau—type instability of a retracting viscous front is controlled by slip on the substrate. We can predict the characteristic stages of the evolution of the dewetting film within the framework of a single thin-film model. This unified description connects the different morphological transitions seen in our experiments, in particular, (i) for no (or weak) slip, the occurrence of a symmetric rim shape with oscillatory decay and a symmetric instability, (ii) for strong slip, a monotonic to oscillatory transition of the cross-sectional rim shape towards a profile with asymmetric bulges. Within the experimental error bars, the characteristic wavelength of the fastest rim undulation λ is unaffected by slip. The rise time of the bulge growth, however, is lowered with increasing slip and serves as a striking feature for slippage of viscous films.

A general conclusion is that liquid slip not only affects the time scales and, hence, the velocities involved in flow processes or—e.g., in microfluidic channels—the throughput, it also has implications on the spatial morphology. In other words, by monitoring a retracting front of a viscous film through an optical microscope, one can judge whether or not slippage is at work.

The authors acknowledge financial support from the German Research Foundation (DFG) within the framework of the priority program SPP 1164 (JA 905/3), graduate school GRK 1276, BA 3406/2, and Matheon.

O. Bäumchen and L. Marquant contributed equally to this work.

*k.jacobs@physik.uni-saarland.de
†Present address: Max Planck Institute for Dynamics and Self-Organization (MPIDS), 37077 Göttingen, Germany.

[1] F. Rayleigh, Proc. London Math. Soc. **s1-10**, 4 (1878).
[2] J. Plateau, *Experimental and Theoretical Steady State of Liquids Subjected to Nothing but Molecular Forces* (Gauthier-Villars, Paris, 1873).
[3] J. Eggers, Rev. Mod. Phys. **69**, 865 (1997).
[4] J. Eggers and E. Villermaux, Rep. Prog. Phys. **71**, 036601 (2008).
[5] C. Redon, F. Brochard-Wyart, and F. Rondelez, Phys. Rev. Lett. **66**, 715 (1991).
[6] G. Reiter and A. Sharma, Phys. Rev. Lett. **87**, 166103 (2001).
[7] J.-L. Masson, O. Olufokunbi, and P. F. Green, Macromolecules **35**, 6992 (2002).

[8] P. Damman, N. Baudelet, and G. Reiter, Phys. Rev. Lett. **91**, 216101 (2003).
[9] B. M. Besancon and P. F. Green, Phys. Rev. E **70**, 051808 (2004).
[10] A. Sharma and G. Reiter, J. Colloid Interface Sci. **178**, 383 (1996).
[11] S.-H. Choi and B. Z. Newby, J. Chem. Phys. **124**, 054702 (2006).
[12] F. Brochard-Wyart and C. Redon, Langmuir **8**, 2324 (1992).
[13] A. Münch and B. Wagner, J. Phys. Condens. Matter **23**, 184101 (2011).
[14] J. H. Snoeijer and J. Eggers, Phys. Rev. E **82**, 056314 (2010).
[15] A. Oron, S. H. Davis, and S. G. Bankoff, Rev. Mod. Phys. **69**, 931 (1997).
[16] R. V. Craster and O. K. Matar, Rev. Mod. Phys. **81**, 1131 (2009).
[17] R. Seemann, S. Herminghaus, and K. Jacobs, Phys. Rev. Lett. **86**, 5534 (2001).
[18] P.-G. de Gennes, Rev. Mod. Phys. **57**, 827 (1985).
[19] A. Sharma and K. Kargupta, Appl. Phys. Lett. **83**, 3549 (2003).
[20] O. Bäumchen and K. Jacobs, J. Phys. Condens. Matter **22**, 033102 (2010).
[21] S. Gabriele, S. Sclavons, G. Reiter, and P. Damman, Phys. Rev. Lett. **96**, 156105 (2006).
[22] L. Bocquet and J.-L. Barrat, Soft Matter **3**, 685 (2007).
[23] E. Lauga, M. P. Brenner, and H. A Stone, in *Handbook of Experimental Fluid Mechanics*, edited by C. Tropea, A. Yarin, J. F. Foss (Springer, New York, 2007), Chap. 19.
[24] T. M. Squires and S. R. Quake, Rev. Mod. Phys. **77**, 977 (2005).
[25] D. C. Tretheway and C. D. Meinhart, Phys. Fluids **14**, L9 (2002).
[26] J. D. McGraw, J. Li, D. L. Tran, A.-C. Shi, and K. Dalnoki-Veress, Soft Matter **6**, 1258 (2010).
[27] A. G. González, J. A. Diez, and L. Kondic, J. Fluid Mech. **718**, 246 (2013).
[28] C. L. M. H. Navier, Mem. Acad. Sci. Inst. Fr. **6**, 389 (1823).
[29] M. Lessel, O. Bäumchen, M. Klos, H. Hähl, R. Fetzer, R. Seemann, M. Paulus, and K. Jacobs, arXiv:1212.0998.
[30] R. Fetzer, K. Jacobs, A. Münch, B. Wagner, and T. P. Witelski, Phys. Rev. Lett. **95**, 127801 (2005).
[31] O. Bäumchen, R. Fetzer, and K. Jacobs, Phys. Rev. Lett. **103**, 247801 (2009).
[32] O. Bäumchen, R. Fetzer, A. Münch, B. Wagner, and K. Jacobs, in *IUTAM Symposium on Advances in Micro- and Nanofluidics*, edited by M. Ellero, X. Hu, J. Fröhlich, and N. Adams (Springer, Dordrecht, 2009), p. 51.
[33] O. Bäumchen, R. Fetzer, M. Klos, M. Lessel, L. Marquant, H. Hähl, and K. Jacobs, J. Phys. Condens. Matter **24**, 325102 (2012).
[34] P. Gutfreund, O. Bäumchen, R. Fetzer, D. van der Grinten, M. Maccarini, K. Jacobs, H. Zabel, and M. Wolff, Phys. Rev. E **87**, 012306 (2013).
[35] See Supplemental Material at http://link.aps.org/supplemental/10.1103/PhysRevLett.113.014501 for tabulated substrate (surface and sub-surface) parameters, for a quantification of dewetting velocities including a comparison of morphological features, and for a derivation of the extension of the BWR model, which includes Refs. [36–40].
[36] O. Bäumchen and K. Jacobs, Soft Matter **6**, 6028 (2010).
[37] J. Brandrup, E. H. Immergut, and E. A. Grulke, *Polymer Handbook* (John Wiley & Sons Inc., New York, 1999), 4th ed.
[38] A. Münch, J. Phys. Condens. Matter **17**, S309 (2005).
[39] K. Sekimoto, R. Oguma, and K. Kawasaki, Ann. Phys. (N.Y.) **176**, 359 (1987).
[40] F. Brochard-Wyart, P.-G. de Gennes, H. Hervet, and C. Redon, Langmuir **10**, 1566 (1994).
[41] A. Münch, B. Wagner, and T. P. Witelski, J. Eng. Math. **53**, 359 (2005).
[42] R. Fetzer and K. Jacobs, Langmuir **23**, 11617 (2007).
[43] While b does not appear to be very small compared to the thickness of the film ($b/H \sim 0.4$), to assess the influence of slip on the shape of the rim it is more appropriate to compare b to the height of the rim or the bulges, which are significantly larger than H in the later stages of the evolution. Thus we expect the profiles with large rims or bulges to approach the shape of no-slip profiles, which is symmetric.
[44] J. C. Flitton and J. R. King, J. Eng. Math. **50**, 241 (2004).
[45] Although the comparison between 2D simulation and experiment becomes less obvious for larger D since the unstable film structures acquire a strict 3D shape, we include a simulation result for larger D (59 μm) in Figs. 2(e) and 2(g) which qualitatively follows the experimentally observed behavior (consistently recorded at the peak positions perpendicular to the ridge) in Figs. 2(a) and 2(c) for substantially smaller D (24 μm). Therefore, while a fuller agreement with experiment would require a 3D numerical approach, the qualitative behavior is already captured by the 2D case.
[46] Notice that while the earlier profiles in Figs. 2(d) and 2(h) are in good agreement, the later stages differ due to the growing rim instability, which inflates the profiles in the experimental cross sections, as these are taken at the peaks. Nevertheless, these later stage profiles continue to converge to the symmetric limiting shape predicted by the 2D theory, as seen in Fig. 2(b).